

# IMPACT ASSESSMENT OF ASPHALT CONCRETE IN GEOGRID-REINFORCED-PILE- SUPPORTED EMBANKMENT DURING HIGH- SPEED TRAIN TRAFFIC

ISHOLA VALERE LOIC CHANGO<sup>1\*</sup>,  
GOUBI CYRIAQUE ASSOGBA<sup>2</sup>,  
MUHAN YAN<sup>1</sup>, LING XIANZHANG<sup>1</sup>,  
JOSUE GIRECE MITOBABA<sup>1</sup>

<sup>1</sup>*School of Civil Engineering,  
Harbin Institute of Technology, Harbin, China*

<sup>2</sup>*School of Transportation Science and Engineering,  
Harbin Institute of Technology, Harbin, China*

Received 1 February 2021; accepted 19 May 2021

**Abstract.** Railroad structural behaviour is a significant factor for safety and comfort during high-speed train operation. Intending to improve railway performance, increase its bearing capacity, and reduce vibrations induced by train passage, asphalt concrete has become a material to be integrated into railway construction. Despite several studies evaluating asphalt concrete effect on the railway mechanical behaviour, its impact assessment remains poorly understood. This study investigates the impact of asphalt concrete material in the geogrid-reinforced-pile-supported embankment structure subjected to

\* Corresponding author. E-mail: [chanshola@hit.edu.cn](mailto:chanshola@hit.edu.cn)

Ishola Valere Loic CHANGO (ORCID ID 0000-0001-9169-0622)

Ogoubi Cyriaque ASSOGBA (ORCID ID 0000-0002-1581-5187)

Muhan YAN (ORCID ID 0000-0002-5213-0144)

Ling XIANZHANG (ORCID ID 0000-0002-0384-9232)

Josue Girece MITOBABA (ORCID ID 0000-0002-4490-076X)

Copyright © 2022 The Author(s). Published by RTU Press

This is an Open Access article distributed under the terms of the Creative Commons Attribution License (<http://creativecommons.org/licenses/by/4.0/>), which permits unrestricted use, distribution, and reproduction in any medium, provided the original author and source are credited.

high-speed train moving. A 3D nonlinear finite element model was developed to simulate Harbin (Dalian (China) instrumented railroad test section accurately. The high-speed train moving load was modelled as a transitory dynamic load via a user-defined subroutine 3D load in which the track irregularity is incorporated. The established model was effectively validated by the vibration acceleration and stress measured in the field test section. The asphalt concrete viscoelasticity behaviour was incorporated into the 3D geogrid-reinforced-pile-supported embankment finite element model through the Prony series to characterise its mechanical response better. The impact of asphalt concrete material in maintaining a low and constant structural vibration, regardless of train weight level, moving speed variations, and weather conditions were investigated, analysed and discussed.

**Keywords:** 3D-railway finite element model, asphalt concrete, dynamic response, finite element model (FEM), railway system, train moving load.

## Introduction

The rail transportation networks have made enormous progress in reducing commute times and ensuring passenger safety. However, minimizing structure vibration to improve passenger comfort remains a fundamental concern in research. Some studies were conducted to optimize the dynamic of railway system response through the structural design, maintenance and modernization of the railroad system for high-speed trains (Chango et al., 2019; Gailienė & Ramūnas, 2019; Liu & Shao, 2011; Zakeri et al., 2017). Through the experimental test, Sysyn et al. (2019) showed that the ballast layer consolidation significantly influences the distribution of stresses under the sleeper.

Asphalt material was integrated into railroad structures design and construction to achieve very high levels of railway performance while reducing long-term maintenance costs and increasing service life. The main advantages of this practice are the provision of additional support to improve the load distribution capabilities of the railroad system and the reduction of the pressure on the foundation layer caused by the dynamic load (Rose, 2013).

Numerous studies have been oriented on the importance of the asphalt concrete (AC) material in improving high-speed railway performance. Using numerical and experimental models, Yang et al. (2015) found that replacing the embankment top portion with an AC layer improved the structure stability and reduced deformations. The positioning of the AC material at the ballasted trackbed down is efficient because of the minimal vibrations observed in the system and the trackability to withstand more stress under dynamic train loads (Fang et al., 2013). Regarding the type of asphalt, Lee et al. (2014), based

on laboratory results, revealed that asphalt mixtures with styrene-butadiene-styrene (SBS) and crumb rubber modifier (CRM) asphalt binders could increase the railway system performance. These earlier studies focused on the AC material influence on the railway system, but the AC effect on the system vibration is still poorly understood.

Furthermost, the numerical analysis evaluating the effect of asphalt on the railway structure has considered it in the linear elastic state. In contrast, asphalt concrete behaves elastically at high loading speeds or low temperatures (Yusupov et al., 2020). Devecseri (2010) also showed that asphalt concrete behaves differently after burning at high temperatures. Thus, using the behaviour of viscoelastic materials for the AC layer in a railway structure provides accurate results in terms of dynamic responses. Furthermore, the ability of AC material to maintain the structure vibrations, constant and low, despite the train speed variation during its operation, is still unknown and must be investigated.

## 1. Objectives and scope

The main objective of this study is to evaluate the AC material impact in a geogrid-reinforced-pile supported embankment (GRSP) railroad structure dynamic response. A 3D nonlinear finite element model (FEM) of a GRSP system was established through the Abaqus program to achieve the purpose (Abaqus, 2011). The high-speed train (HST) moving wheel load has been performed as a transitory dynamic load implemented via a user-defined Fortran subroutine (Chango et al., 2019). The viscoelastic behaviour of asphalt concrete material was incorporated into the model for further accurate characterisation of its dynamic properties. The finite element model reliability was confirmed by comparing the calculated results with the dynamic stress and vibration accelerations measured in China Harbin–Dalian high-speed line railway section. Thereafter, the impact of the AC layer on the railway

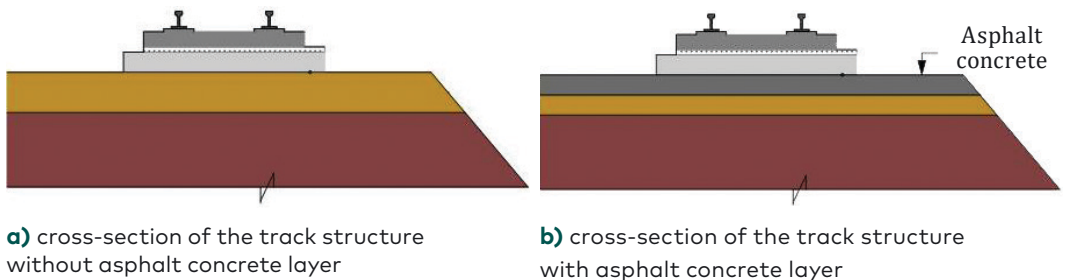


**Figure 1.** Track structure cross-section

system dynamic response was evaluated. Finally, the weather conditions consequence on the AC layer performance (Figure 1) in the railway system was also analysed by considering three types of climates.

## 2. Numerical model of the geogrid-reinforced-pile supported embankment railway system

This section describes the railroad structure FEM, whose embankment was reinforced by two layers of geogrid and the ground enhanced by some CFG piles and the moving HST load.

### 2.1. Establishment of the 3D nonlinear finite element of the instrumented section

#### 2.1.1. Model description

The developed FEM was based on the railway section of Harbin-Dalian, a 13.6 m wide double track. The embankment height was 5.433 m, and its slope factor was 1:1.5. The trackbed is a type-I CRTS model, which includes the fastener system, the CN60 rails, the track slab, the cement asphalt mortar, the resin material and the concrete roadbed (Yang et al., 2016). The track embankment consists of a well-graded gravel layer, standard A/B group fill layer; NFH (non-frost heaving) group filling A/B; standard A/B/C group fill; and cushion crushed layer in which two membranes of geogrid are positioned. The ground, reinforced by CFG (cement fly-ash gravel) piles to support the embankment, consists of loess clay 10 m thick, silty clay 10 m thick and silt 12 m thick. All piles, each 20 m in length and 0.5 m in diameter are arranged in an equilateral triangle with a spacing of 1.5 m (Chango et al., 2019).

The tested section geometry was reduced to half in this developed FEM in Abaqus (Abaqus, 2011). Thereby, the size of the model is 125 m in length and 20 m wide. A reciprocated interaction between the track components and the embankment has been ensured by using a tie link. The rail was modelled by adopting the beam element Euler-Bernoulli and the geogrids were implanted into the cushion crushed layer (Chen & Zhou, 2018). In this model, the fastener system, modelled as a spring-damper, was assumed to be linear with 45 kN/mm stiffness. The damping is supposed to be proportional to the deformation rate of the rail pad, and its value was 45 kN-s/m. A Cartesian-coordinate system was adopted as follows:

- the x axis represents the transverse direction of the railway;
- the y axis represents the vertical direction;
- the z axis represents the longitudinal direction of the HST motion, as shown in Figure 2.

### 2.1.2. Finite element model mesh and boundary condition

The mesh has been defined differently to simulate structural dynamic behaviour to respect the computes convergences correctly. Thus, the area under the HST load application surface is described by a fine mesh, while a dense mesh defines the area near the HST load application surface. A relatively coarse mesh describes the far region area.

All solid section meshes are eight nodes linear brick with hourglass control and reduced integration. The 4-node quadrilateral membrane

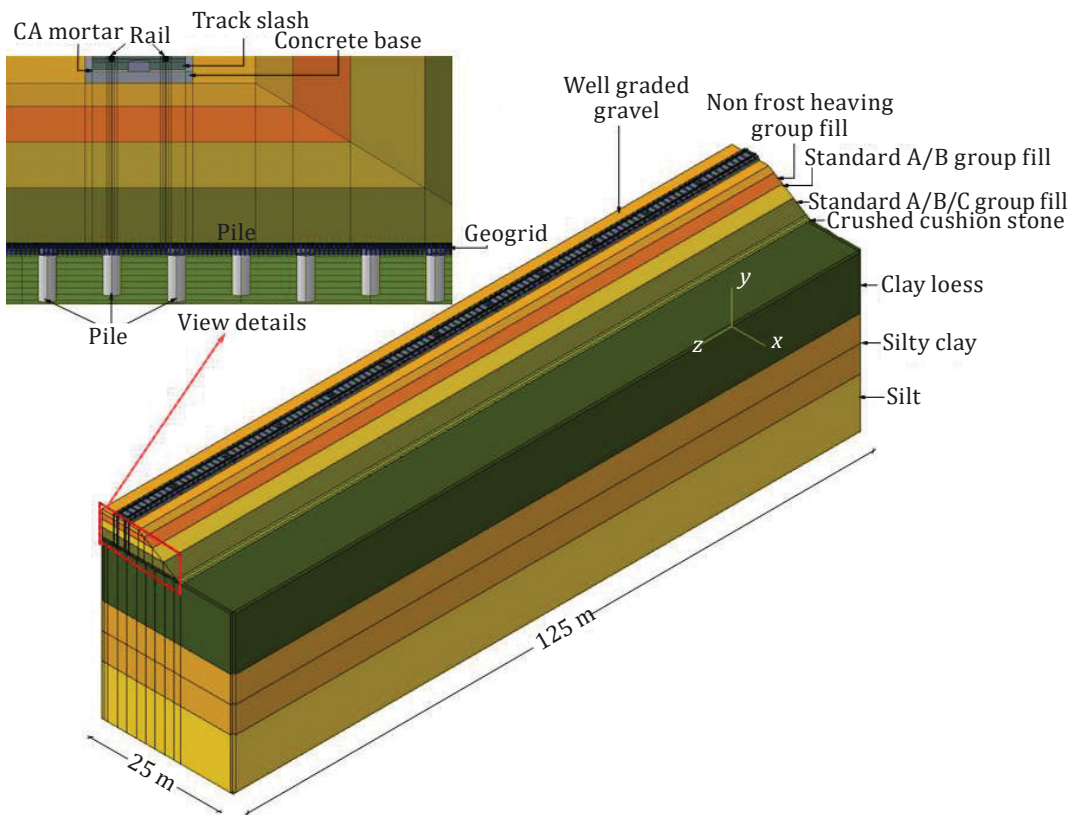


**Figure 2.** 3D Harbin-Dalian railway model

with hourglass control and reduced integration was used to describe the geogrid mesh (Chango et al., 2019; Zienkiewicz et al., 2005). The division of the FEM into two equal parts of the tested section geometry makes it possible to restrain any X-direction translation to symmetry boundary. Due to the structural problems of dynamic behaviour, the infinite boundary conditions were used on the remaining outer faces to reduce the reflection consequence of the waves and absorb all stress waves around the boundary surface to ensure accuracy in the results, as shown in Figure 3.

### 2.1.3. Induced dynamic load modelling

During the HST motion along the rail, its load is considered a dynamic and static change combination. A dynamic load generates a local increase in the complete train load because of its uneven reaction to the rails. The dynamic HST load is often affected by railroad profile irregularities, the HST suspension systems, and the moving HST speed. Thus, it is made simpler by the continuous loading amplitude variation through Equation (1), which is solved by an implicit method:

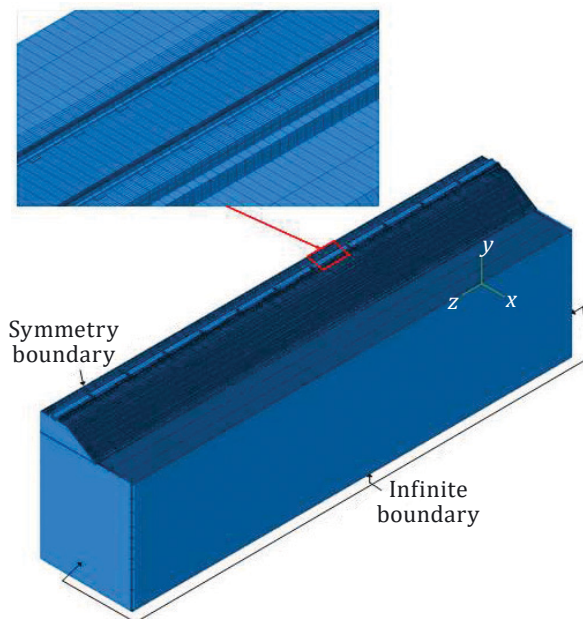


**Figure 3.** The 3D mesh of the finite element model

$$[M]\{\ddot{U}\} + [C]\{\dot{U}\} + [K]\{U\} = \{P\}, \quad (1)$$

where  $[M]$  – mass matrix;  $[C]$  – damping matrix;  $[K]$  – stiffness matrix;  $\{P\}$  – external force vector;  $\{\ddot{U}\}$  – an acceleration vector;  $\{\dot{U}\}$  – velocity vector;  $\{U\}$  – displacement vector.

During field tests, the CRH3 HST model was used. In this study, it is supposed that each train carriage, whose components are considered rigid parts connected by damper-spring elements, is flawlessly proportioned. The connection of the different train carriage parts is described in Figure 4. To specify non-uniform distributed HST load (DLOAD), the dynamic force due to train movement upon the rail has been developed as a transitory local dynamic load via a subroutine. This method allows operators to specify the magnitude change of the scattered load as time function form (TIME\*), coordinates (COORDS\*), load integration point number applied and domain element number (Assogba et al., 2021; Chango et al., 2019). The simplification of the calculation methods has led to the assumption that the HST wheels and the rails always contact each other, which means an inexistence of relative vertical displacement during the operation.

The rail irregularity is regularly modelled as a single or compound concave cosine wave (Gao & Zhai, 2014). Thus, it is supposed that the existence of a cosine track irregularity ( $Z_w$ ) at the rail surface with an amplitude  $A$  and a wave number  $k_x$  using Equation (2):

$$k_x = \frac{2\pi}{\lambda}, \quad (2)$$

where  $\lambda$  is the wavelength.

The track irregularity is defined as follows (Equation (3)):

$$z_w(t) = A(1 - \cos(k_x t)). \quad (3)$$

The high-speed train model, composed of three wagons for the test, is established based on the quarter-carriage model. Each carriage contains two bogies, including two wheelsets per bogie. Thus, the wheel-rail contact force taking into account the irregularities of the track, defined in (Bian et al., 2015), was expressed as follows (Equation (4)):

$$p(y, t) = \sum_{n=1}^3 \sum_{i=1}^4 p_{n_i}(y - vt), \quad (4)$$

where  $x$  represents the distance between the train axle and a reference point at the train head;  $v$ ,  $t$  and  $i$  represent the train speed, the time and the axles numbering in a carriage, respectively;  $p_{n_i}(y - vt)$  represents the  $i^{\text{th}}$  wheels pair in the  $n^{\text{th}}$  carriage wheel-rail contact force.

$$\sum_{i=1}^4 p_{n_i} (y-vt) = p_{n_1} \delta \left( y-vt + \sum_{n=1}^{q=0} L_q + L_0 \right) + p_{n_2} \delta \left( y-vt + c_n + \sum_{n=1}^{s=0} L_q + L_0 \right) + p_{n_3} \delta \left( y-vt + c_n + d_n + \sum_{n=1}^{s=0} L_q + L_0 \right) + p_{n_4} \delta \left( y-vt + 2c_n + d_n + \sum_{n=1}^{s=0} L_q + L_0 \right), \quad (5)$$

where  $L_0$  represents the distance between a reference point in the running direction and the train head;  $L_q$  represents the  $(n - 1)^{th}$  length of a carriage;  $c_n$  and  $d_n$  represent the distance between two-wheel axles in the  $n^{th}$  carriage and the distance between an axle and the following one in  $n^{th}$  carriage bogies;  $\delta$  represents a Dirac Delta function.

Substituting Equation (5) into the quarter-carriage model and the following expression (Equation (6)) was obtained:

$$p_{n_i} (k_x, \omega) = W_{n_1} \delta(\omega - k_x v) + W_{n_2} \delta(\omega - \omega_r - k_x v) + W_{n_3} \delta(\omega + \omega_r - k_x v), \quad (6)$$

where  $\delta$  represents a Dirac Delta function and  $\omega_r$ . The excitation frequency due to rail surface irregularity is defined by  $\omega_r = 2\pi v / \lambda$ ;  $\lambda$  the rail wavelength.

The  $i^{th}$  HST wheel transient dynamic at a position  $x$ , established via Fortran and integrated into the implicit analysis, was defined through Equation (2) and Equation (5) combination. The equivalent parameters of the train model were recapped in Table 1.

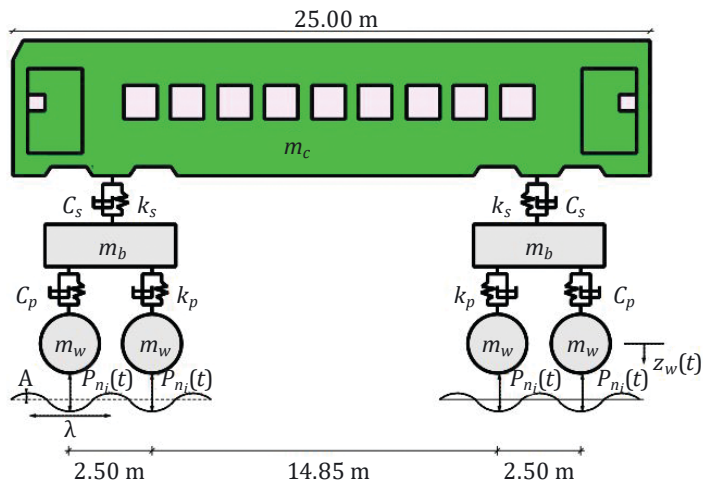


Figure 4. Train model used geometry

## 2.1.4. Material structural damping

Any structure subjected to a dynamic load is most often influenced by various materials damping properties. Thus, the damping accuracy of materials is essential in structural behaviour prediction. However, the difficulty of accurately determining the damping matrix in a FE analysis must be emphasized. In this work, Rayleigh Damping has been utilized and expressed in Equation (6):

$$[C] = \alpha[M] + \beta[K], \quad (6)$$

where  $[C]$  – the physical system damping matrix;  $[M]$  – physical system mass matrix;  $[K]$  – system stiffness matrix;  $\alpha$  and  $\beta$  – the predefined constants.

The damping coefficients are calculated as a function of the damping ratio and the natural frequency of the structure. Thus,  $\alpha$  and  $\beta$  are expressed as follows (Equations (7) and (8)):

$$\alpha = \frac{2\omega_1\omega_2}{\omega_1 + \omega_2} \xi_0, \quad (7)$$

$$\beta = \frac{2}{\omega_1 + \omega_2}, \quad (8)$$

where  $\xi_0$  – damping ratio.

The method used to calculate the Rayleigh damping parameters is stated as follows. Initially, a modal analysis was carried out on the numerical model implemented in Abaqus (Abaqus, 2011). The first 40 natural circular frequencies have been taken out to define the

**Table 1. The equivalent of the train model parameters**

<b>Designation</b>	<b>Value</b>
Carriage mass, kg	$40 \cdot 10^3$
Bogie mass, kg	$3.20 \cdot 10^3$
Wheel axle mass, kg	$2.40 \cdot 10^3$
Axle load, kN	$0.14 \cdot 10^3$
Wheel axle distance in a bogie, m	2.50
Bogies distance in a wagon, m	14.85
Carriage length, m	25.00
Primary suspension spring stiffness, kN/m	2080
Primary suspension spring damping	$100 \cdot 10^3$
Secondary suspension spring stiffness, kN/m	800
Primary suspension spring damping	$120 \cdot 10^3$

fundamental frequency  $\omega_1$ . Once the fundamental frequency has been defined, the second circular frequency  $\omega_2$  has been chosen from among the higher-order vibration modes. As a result, the circular frequencies  $\omega_1$  and  $\omega_2$  determined for calculating the Rayleigh damping parameters are 16.261 rad/s and 18.912 rad/s. In this paper, the damping ratio  $\xi$  for the structure was selected within 2–4%. Thus, the Rayleigh damping coefficient  $\alpha$  and  $\beta$  of the structure were calculated using Equations (7) and (8) using the abovementioned data. The proportional damping value  $\alpha$  is 0.5269, and the stiffness proportional damping value  $\beta$  is 0.0017.

## 2.2. Geogrid-reinforced-pile-supported embankment material characterisation and properties

### 2.2.1. Non-asphaltic material layer

In this work, the trackbed materials and each embankment material are considered linear elastic, founded on the hypothesis of a flexible layered structure. The elastoplastic behaviour has been integrated into the ground mechanical properties using the Mohr–Coulomb model with a continuous assumption of the interaction between one layer and the following one. The fastening elements connecting the track slab to the rail were modelled as a spring-damper with 45 kN/mm stiffness and a damping coefficient of 45 kN·s/m. Based on preceding works (Sun et al., 2013; Yang et al., 2016), the equivalent materials parameters are recapped in Table 2. Each geogrid layer, considered linear elastic, was modelled as an isotropic membrane with maximum tensile strength and a Poisson ratio of  $30 \cdot 10^3$  N/m and 0.3, respectively. As for the piles, a concrete plasticity damage behaviour was integrated into the pile mechanical properties for the accuracy of its behaviour in the GRSP structure. The pile concrete plastic stress-strain relationship and its concrete damage-strain relationship were recapped in Table 3 (Chango et al., 2019).

Table 2. Materials mechanical properties

Material	Elastic modulus, Pa	Density, g/m <sup>3</sup>	Poisson ratio	Cohesion, 10 <sup>3</sup> Pa	Friction angle, °
Rail	210·10 <sup>9</sup>	7800·10 <sup>3</sup>	0.30	~	~
Track slab	39·10 <sup>9</sup>	2500·10 <sup>3</sup>	0.30	~	~
CA mortar (CAM)	10·10 <sup>7</sup>	1800·10 <sup>3</sup>	0.30	~	~
Concrete base	32.5·10 <sup>9</sup>	2500·10 <sup>3</sup>	0.27	~	~
Graded gravel	310·10 <sup>6</sup>	1800·10 <sup>3</sup>	0.30	~	~
Non-frost heaving group material A/B	298·10 <sup>6</sup>	2060·10 <sup>3</sup>	0.30	~	~
Group material A/B	350·10 <sup>6</sup>	2080·10 <sup>3</sup>	0.30	~	~
Group material A/B/C	298·10 <sup>6</sup>	1980·10 <sup>3</sup>	0.30	~	~
Cushion crushed stone	300·10 <sup>6</sup>	1850·10 <sup>3</sup>	0.30	~	~
Clay loess material	19·10 <sup>6</sup>	1850·10 <sup>3</sup>	0.35	13	12
Silty clay material	19·10 <sup>6</sup>	1650·10 <sup>3</sup>	0.40	11	9
Silt material	27·10 <sup>6</sup>	1880·10 <sup>3</sup>	0.35	17	19

Impact Assessment of Asphalt Concrete in Geogrid-Reinforced-Pile-Supported Embankment During High-Speed Train Traffic

Table 3. Pile mechanical properties with concrete strength C25

Compression hardening		Tension stiffening		Compression damage		Tension damage	
Stress, 10 <sup>3</sup> N/m <sup>2</sup>	Strain	Stress, 10 <sup>3</sup> N/m <sup>2</sup>	Strain	Damage dc	Strain	Damage dt	Strain
11 690.00	0.000	1797.800	0.000	0.000	0.000	0.000	0.000
16 700.00	0.809·10 <sup>-3</sup>	1780.000	0.026·10 <sup>-3</sup>	0.010000	0.809·10 <sup>-3</sup>	0.010000	0.026·10 <sup>-3</sup>
13 239.80	2.340·10 <sup>-3</sup>	1191.06	0.136·10 <sup>-3</sup>	0.207199	2.340·10 <sup>-3</sup>	0.330864	0.136·10 <sup>-3</sup>
9841.27	3.860·10 <sup>-3</sup>	859.483	0.236·10 <sup>-3</sup>	0.410702	3.860·10 <sup>-3</sup>	0.517144	0.236·10 <sup>-3</sup>
7674.36	5.350·10 <sup>-3</sup>	684.527	0.332·10 <sup>-3</sup>	0.540458	5.350·10 <sup>-3</sup>	0.615434	0.332·10 <sup>-3</sup>
6248.49	6.800·10 <sup>-3</sup>	576.455	0.425·10 <sup>-3</sup>	0.697180	6.800·10 <sup>-3</sup>	0.747045	0.425·10 <sup>-3</sup>
5255.01	8.240·10 <sup>-3</sup>	502.469	0.516·10 <sup>-3</sup>	0.786110	8.240·10 <sup>-3</sup>	0.834016	0.516·10 <sup>-3</sup>
4527.98	9.670·10 <sup>-3</sup>	448.233	0.608·10 <sup>-3</sup>	0.841140	9.670·10 <sup>-3</sup>	0.888637	0.608·10 <sup>-3</sup>
3974.73	11.100·10 <sup>-3</sup>	406.519	0.698·10 <sup>-3</sup>	0.877465	11.100·10 <sup>-3</sup>	0.919064	0.698·10 <sup>-3</sup>
3540.40	12.500·10 <sup>-3</sup>	373.278	0.789·10 <sup>-3</sup>	0.902661	12.500·10 <sup>-3</sup>	0.937999	0.788·10 <sup>-3</sup>
		131.570	3.800·10 <sup>-3</sup>			0.998225	3.560·10 <sup>-3</sup>
Elasticity modulus, MPa		2800					
Poisson ratio		0.2					
Dilatation angle		30					
Eccentricity		0.10					
Stress ratio $\sigma_{bo}/\sigma_{co}$		1.16					
Pressure ratio $K_c$		0.667					
Viscosity parameter		0.0005					

### 2.2.2. Viscoelastic asphalt concrete layer

To define its mechanical properties, the asphalt concrete material was considered a thermo-rheological body with linear viscoelastic behaviour. Thus, the constitutive Equation (9) of this type of material is described as follows (Equations (10)–(12)) (Hu et al., 2009):

$$\sigma_{ij}(x_k, \xi) = \int_0^{\xi} c_{ijkl}(\xi - \xi') \frac{\partial \varepsilon_{kl}(x_k, \xi')}{\partial \xi'} d\xi' - \int_0^{\xi} \beta_{ij}(\xi - \xi') \frac{\partial \theta_{kl}(x_k, \xi')}{\partial \xi'} d\xi', \quad (9)$$

with

$$\xi = \xi(t) \equiv \int_0^t \frac{1}{a_T} d\tau, \quad (10)$$

$$\xi' = \xi(t') \equiv \int_0^{t'} \frac{1}{a_T} d\tau, \quad (11)$$

$$\begin{cases} a_T = a_T[T(\tau)] \\ a_T = a_T[\theta(\tau)] \end{cases} \quad (12)$$

where  $a_T$  is the time-temperature shift factor;  $\tau$  is the integration variable;  $t$  and  $t'$  are the time moment;  $\sigma_{ij}$  and  $\varepsilon_{kl}$  are respectively the stress and strain tensor;  $x_k$  is the function of position;  $\beta_{ij}$  is the second-order tensor of relaxation modulus relating thermal strain to stress;  $c_{ijkl}$  is the fourth-order tensor of relaxation moduli relating stress to mechanical strain.

In the FEM, the used viscoelastic property in terms of relaxation is described in hereditary integral form Equations (13) and (14) via Maxwell-kernel functions generalized elements (Minhoto et al., 2008):

$$G(\xi) = G_0 + \sum_{i=1}^{n_G} G_i e^{\left(-\frac{\xi}{\lambda_i^G}\right)}, \quad (13)$$

$$K(\xi) = K_0 + \sum_{i=1}^{n_K} K_i e^{\left(-\frac{\xi}{\lambda_i^K}\right)}. \quad (14)$$

The kernel functions have been stated using an efficient analysis algorithm named Prony–Dirichlet series, whose formulation is stated by Equations (15) and (16):

$$G(t) = G_0 \left[ 1 - \sum_{i=1}^N G_i \left( 1 - e^{\left(-\frac{t}{\tau_i}\right)} \right) \right], \quad (15)$$

$$K(t) = K_0 \left[ 1 - \sum_{i=1}^N K_i \left( 1 - e^{\left( \frac{-t}{\tau_i} \right)} \right) \right], \quad (16)$$

where  $N$  is the number of Prony Dirichlet series terms;  $G_0$  and  $K_0$  are respectively the instantaneous shear modulus and the bulk modulus;  $G_i$ ,  $K_i$  and  $\tau_i$  are the Prony–Dirichlet series factors. Williams–Landel–Ferry function described in Equation (17) was exploited to model the time-temperature superposition of AC materials (Williams et al., 1955):

$$\log(a_T) = \frac{-C_1(T - T_{ref})}{C_2 + (T - T_{ref})}, \quad (17)$$

where  $a_T$  is the time-temperature shift factor;  $C_1$ ,  $C_2$  are the regression factors;  $T$  and  $T_{ref}$  are respectively the analysis and the reference temperature. The regression factors have been obtained from the sigmoid function expressed in Equations (18) and (19):

$$\log(E(t_r)) = \delta + \frac{\alpha}{1 + \exp(\beta + \gamma \log(t_r))}, \quad (18)$$

with

$$a_T = \frac{t}{t_r}, \quad (19)$$

where  $\alpha$ ,  $\beta$ ,  $\gamma$ , and  $\delta$  are the regression coefficients;  $t$  is the time before conversion under the temperature test;  $t_r$  is the time after conversion under reference temperature.

Based on the US standard test method for asphalt dynamic modulus, several dynamic complex modulus experiments were performed to determine the viscoelastic parameters of AC. The tests were performed at various temperatures (–10 °C, 15 °C, 20 °C, 30 °C, and 50 °C), with loading frequencies of 0.01 Hz, 0.10 Hz, 0.20 Hz, 0.50 Hz, 1 Hz, 2 Hz, 5 Hz, 10 Hz, 20 Hz, and 25 Hz for each temperature. The complex dynamic modulus and the phase angle obtained from the experiments were used to determine the relaxation modulus via the approximate method proposed by Park & Schapery (1999) and Schapery & Park (1999). Shear and relaxation moduli were derived from the complex dynamic modulus and the phase angle. Thus, the Prony–Dirichlet series values were obtained by adjusting the test results in the Kernel functions (Equations (15) and (16)). Moreover, the Williams–Landel–Ferry factor could be obtained at different temperatures based on the principle of thermorheological simplicity (Equations (16)–(18)) (Assogba et al., 2020). The instantaneous elastic modulus and the Prony Dirichlet series parameter of the material at the three-temperature test of –10 °C (winter condition), 20 °C (autumn condition), and 50 °C (summer condition) are listed in Table 4.

### 3. Field test process and finite element model reliability verification

#### 3.1. Field test process

The Harbin-Dalian double-line railway was the section instrumented to measure the vibration accelerations of the railroad and the dynamic loading of the rail. Two instruments were used: dynamic stress sensors and accelerometers (Chango et al., 2019). The sensors components for measuring dynamic stress were posed at the rail side. Some accelerometers were posted on the track slab. Other accelerometers were mounted on the shoulder of the embankment, facing the rail fulcrum and close to the concrete base, as described in Figure 5. The accelerometer sensors were TG-1 model manufactured by Beijing Taize Technology Development Co. Ltd, with:

- a frequency range from 0 Hz to 3000 Hz;
- measurable acceleration field ranging from 0.1 g to 10 g;
- linearity of 3% F.S, the sensitivity;
- a sensitivity of 1–2% F.S;
- a working power from 5VDC to 24VDC;

Table 4. Asphalt concrete proprieties under different weather conditions

Prony series parameter											
50 (summer condition)			20 (autumn condition)			-10 (winter condition)					
Shear modulus	Bulk modulus	Time	Shear modulus	Bulk modulus	Time	Shear modulus	Bulk modulus	Time			
G	K	$\tau$	G	K	$\tau$	G	K	$\tau$			
0.45334	0.45334	$10^{-5}$	0.09236	0.09236	$10^{-5}$	0.00530	0.00530	$10^{-5}$			
0.21401	0.21401	$10^{-4}$	0.08712	0.08712	$10^{-4}$	0.00509	0.00509	$10^{-4}$			
0.17327	0.17327	$10^{-3}$	0.14720	0.14720	$10^{-3}$	0.01120	0.01120	$10^{-3}$			
0.08664	0.08664	$10^{-2}$	0.20840	0.20840	$10^{-2}$	0.02075	0.02075	$10^{-2}$			
0.03570	0.03570	$10^{-1}$	0.21063	0.21063	$10^{-1}$	0.04483	0.04483	$10^{-1}$			
0.01373	0.01373	1	0.13729	0.13729	1	0.07465	0.07465	1			
0.00586	0.00586	10	0.06266	0.06266	10	0.15456	0.15456	10			
0.00240	0.00240	$10^2$	0.02341	0.02341	$10^2$	0.16654	0.16654	$10^2$			
0.00154	0.00154	$10^3$	0.01228	0.01228	$10^3$	0.30576	0.30576	$10^3$			
Elasticity modulus, MPa			1472.60			9217.60			21906.30		
Poisson Ratio			0.25			0.25			0.25		

- an output voltage range from 0.5 V to 4.5 V;
- an operating temperature was varying from 40 °C to 105 °C.

The sensor of dynamic stress was a DH1205 78 mm gauge length with 350 Ω of resistance; a range of operating temperature from -20 °C to +80 °C, and designed by Jiangsu Donghua Testing Technology Co. Ltd.

A CRH3 train model consisting of three wagons was used at various speeds (200 km/h, 260 km/h, and 300 km/h) with the same axle loading. The instrumentation data has been recorded using an electronic data acquisition system.

### 3.2. Finite element model reliability verification

This work was necessary to check the developed FEM reliability to accurately predict the GRSP structure dynamic behaviour generated by the transient load of the moving HST. Thus, the recorded data from the field tests were compared with the one computed through the numerical model. The stress at the rail side and the vibration accelerations at the embankment and the track slab were measured by the sensors during the test, which first took place at 200 km/h, then at 260 km/h and finally at 300 km/h (moving train speed).

In this study, the field measurements were compared to the FEM results at the HST speed of 300 km/h, as depicted in Figures 6–8.

In Figure 6, there is a high similarity between the dynamic stress applied on the rail side measured on the field and calculated using the FEM. The two curves, having almost the same shape, have a pace that evolves similarly in time, with a peak appearing every time the HST wheel is at the location point. The maximum dynamic stress measured on the field was  $9.28 \cdot 10^3$  kPa, while the one calculated through the FEM

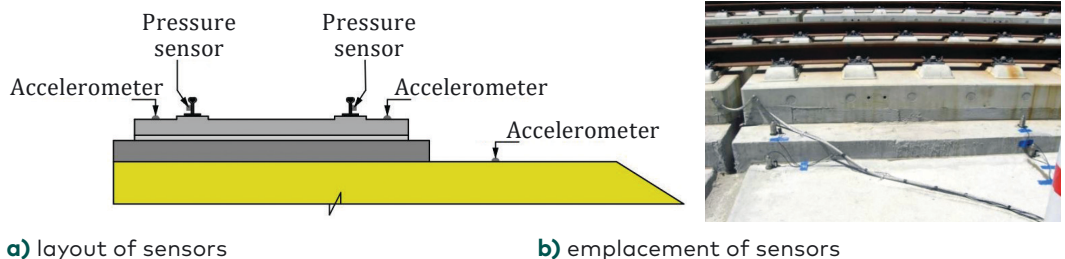
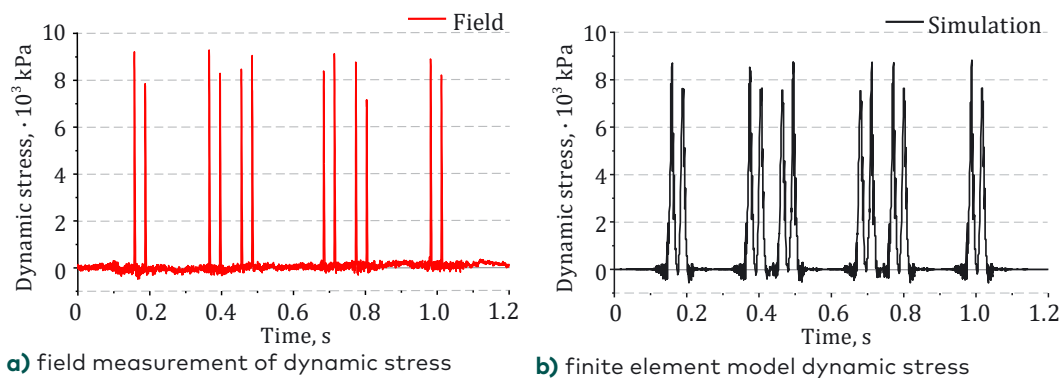


**Figure 5.** Test process at Harbin–Dalian high-speed railway line

was  $8.83 \cdot 10^3$  kPa. Thus, a slight error of 4.32% proves that the FEM predict the existing contact force between the HST wheel and the rail during operation.

The dynamic accelerations at the track slab layer and the embankment are illustrated in Figures 7 and 8. For both figures, the appearance of a wave peak series is observed periodically. This magnitude amplification of these waves at a certain period corresponds to the dynamic effect generated by each HST bogie when it is in contact with a specific location. Besides, a high similarity has been found between the field data and the FEM computed results. In Figure 7, the maximum dynamic acceleration measured on the field and the computed maximum dynamic acceleration were  $1.46 \text{ m/s}^2$  and  $1.38 \text{ m/s}^2$ , respectively. The minimum dynamic acceleration measured on the field and the computed maximum dynamic acceleration were  $-1.05 \text{ m/s}^2$  and  $-1.14 \text{ m/s}^2$ , respectively. The reported difference is, on average, 5.47%. In Figure 8, the maximum dynamic acceleration measured on the field and the computed maximum dynamic acceleration were  $1.22 \text{ m/s}^2$  and  $1.14 \text{ m/s}^2$ , respectively. The minimum dynamic acceleration measured on the field and the computed minimum dynamic acceleration were  $-1.02 \text{ m/s}^2$  and  $-0.93 \text{ m/s}^2$ , respectively. Here, the reported difference is, on average, 7.69%. The probable causes of these noted differences could be related to some conditions described as follow:

1. During the operation, the selected speed vacillated due to the difficulty of keeping the train running speed stable;
2. When approaching a train wheel, the sensors are subjected to vibration and remain subjected even after the wheel passage. Thus, the response of the sensor is affected. That explains the reason for the difference between the spikes slope of the



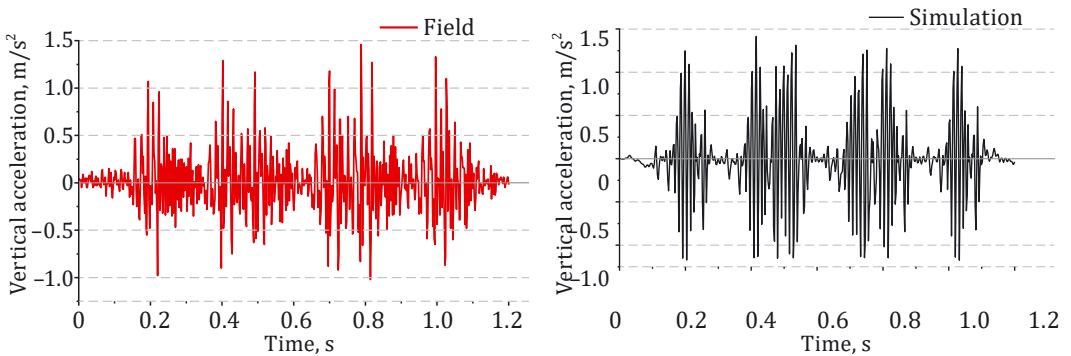
Note: target train speed – 300 km/h; wheel load – 70 kN.

**Figure 6.** The stress at the rail side at a high-speed train speed of 300 km/h

numerical model vibration acceleration and the field measurement vibrations acceleration;

3. It was assumed that the controlled train wheel loads were evenly distributed over a contact area between each train wheel and the rails.

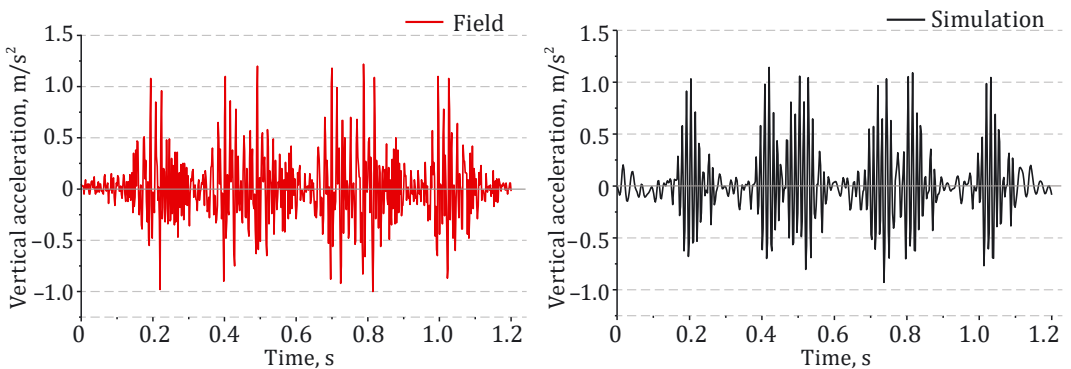
Another reason for the difference between the spikes slope of the numerical model vibration and the field measurement vibrations is to calculate the Rayleigh damping parameters based on a modal analysis carried out on the numerical model to extract the natural circular frequencies of the whole structure. Thus, the natural circular frequencies were determined to calculate the Rayleigh damping parameters. The difference in this procedure is that on-site, each material reacts depending on its damping. In contrast, average damping



**a)** field measurement vertical acceleration      **b)** finite element model vertical acceleration

Note: target train speed – 300 km/h; wheel load – 70 kN.

**Figure 7.** Dynamic acceleration at the track slab top



**a)** field measurement vertical acceleration      **b)** finite element model vertical acceleration

Note: target train speed – 300 km/h; wheel load – 70 kN.

**Figure 8.** Dynamic acceleration at the embankment top

was used for the whole structure in the numerical model, which impacted the numerical results.

An auspicious agreement was obtained between the FEM results and the field test data considering all the above mentioned factors. Hence, the 3D FEM establishment for predicting the GRSP railway system dynamic response under a transitory dynamic train load by considering the rail top surface irregularity is appropriate.

### 3.3. Correlation analysis between field data test and numerical results

To investigate the impact of these observed differences on the accuracy of the structural behaviour prediction model, a correlation study was performed considering all variables of each graph with a sampling frequency of 417.5 samples per second.

The comparative analysis between numerical results and field test data shows that the 3D FEM implemented in Abaqus (Abaqus, 2011) accurately predicts the GRSP railroad system dynamic response. Nevertheless, there is a slight error margin concerning the curve magnitude and shape. To investigate the impact of these observed differences on the accuracy of the structural behaviour prediction model, a correlation study was performed considering all variables of each graph with a sampling frequency of 417.5 samples per second. The stress and the vibration accelerations measured from the field tests and computed through the FEM were processed. The correlation between two variables  $u$  and  $v$  are established by calculating a coefficient  $\Upsilon_{uv}$ :

$$\Upsilon_{uv} = \frac{\sum(u_i - \bar{u})\sum(v_i - \bar{v})}{\sqrt{\sum(u_i - \bar{u})^2} \sqrt{\sum(v_i - \bar{v})^2}}, \quad (20)$$

where  $\bar{u} = 1/n \sum_i^N u_i$  represents the mean of  $u$ ; and  $\bar{v} = 1/n \sum_i^N v_i$  represents the mean of  $v$ .

The Pearson coefficient of correlation calculation results in the interval  $[-1; 1]$ ; the sign indicates the relationship direction. However,  $r=0$  implies the absence of a linear correlation. The level of correlation between the computed results through the FEM and the field data measured has been recapped in Table 5.

The correlation matrix of the stress and accelerations measured from the field test and the FEM results shows that the correlation factor varies from 0.982 to 0.997, depending on location. Thus, the GRSP railway system dynamic response calculated via the FEM and measured on the field at various locations has a significant correlation at the 0.001 level. Therefore, the difference between the FEM results and the field data

concerning the shape and magnitude of the curve is insignificant in influencing the ability of FEM to accurately predict the GRSP railway system subjected to an HST moving load.

## 4. Impact assessment of asphalt concrete in the dynamic railroad response

A 0.2 m thick AC layer has replaced a portion of the embankment top layer to assess the AC material performance in a railway structure. This type of thickness was chosen following Fang & Cerdas (2015) (Figure 1) work, which showed that beyond 0.2 m thick, the impact of the asphalt thickness on the improvement of structure performance becomes scanty. Thus, this structure was compared to the GRSP system without an AC layer at an HST speed of 200 km/h.

### 4.1. Dynamic displacement analysis

The impact of the AC material on the railway system has been investigated. The vertical dynamic displacement curves at the rail up surface are shown in Figure 9. The easily identifiable position of each carriage wheel perfectly matches the geometry of the CRH3 model used, the vertical dynamic displacement for the GRSP structure with AC layer case below the vertical dynamic displacement of the standard GRSP structure. The peak dynamic displacement for the GRSP structure with the AC layer and the standard structure is 1.46 mm and 1.59 mm, respectively. The displacement enhancement rate is 8.17%. Fang et al. (2011) also found that the deformation of a structure with a hot mix asphalt layer positioned above the embankment was slightly inferior

Table 5. Correlation matrix of field data and finite element model

Field measurement	Numerical model			Sig (2-tailed)
	Dynamic stress rail flank	Acceleration track slab up	Acceleration embankment up	
Dynamic stress at rail flank	0.997**			0.000
Acceleration at track slab up		0.982**		0.000
Acceleration at embankment up			0.987**	0.000

to the deformation of the structure without hot mix asphalt. Figure 10 shows the maximum vertical structure displacement with depth. The maximum dynamic displacement decreases rapidly with depth. The maximum dynamic displacement of the GRSP structure with the AC layer was smaller than that of the standard GRSP structure from the rail top. Both maximum displacements began to be close from 25.8 m depth, the piles down. The reduction in GRSP structure displacement during the HST passage is caused by the AC layer, which acts as a rigid platform capable of slowing the wave propagation induced by the HST in the system. Incorporating the AC layer in a GRSP railway structure improves the vibration characteristics of the entire system, increasing its rigidity to withstand dynamic induced loads.

Besides, during the analysis, an attenuation factor of the vibration  $k$  with the depth was defined to clarify the AC material impact better the GRSP railway system. Thus,  $k$  is calculated as follows (Equation (21)):

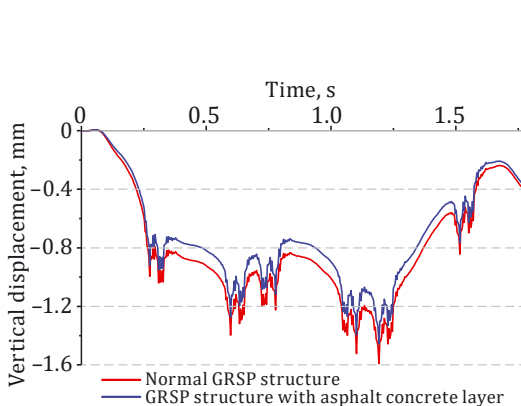
$$k = \frac{U_x}{U_0}, \quad (21)$$

where  $U_0$  – the vertical dynamic displacement maximum value at the rail top (1.589 mm for the standard GRSP structure and 1.457 mm for the GRSP structure with AC layer) and  $U_x$  – the vertical dynamic displacement maximum value at any depth.

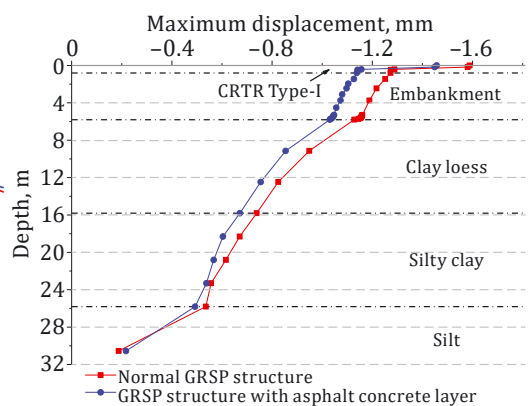
At depth 0.42 m, located at the track slab down, the vertical dynamic displacement of the standard GRSP structure and GRSP structure with AC layer is 1.29 mm and 1.13 mm, respectively. Thus, the vibration attenuation factor for the standard GRSP structure and the GRSP structure with an AC layer is 0.811 and 0.774. For the standard GRSP structure, the dynamic displacement at the track slab is about 81.1% of the dynamic displacement at the rail up. For the GRSP structure with an AC layer, the dynamic displacement at the track slab is about 77.4% of the dynamic displacement at the rail up. At depth 5.23 m, located in the embankment just above the first layer of geogrid, the vertical dynamic displacement of the standard GRSP structure and the GRSP structure with AC layer is 1.18 mm and 1.02 mm, respectively. Thus, the vibration attenuation factor for the standard GRSP structure and the GRSP structure with an AC layer is 0.742 and 0.698, respectively. For the standard GRSP structure, the dynamic displacement at the located position above the geogrid is about 74.2% of the dynamic displacement at the rail up. For the GRSP structure with the AC layer, the vibration at the position above the geogrid is about 69.8% of the vibration at the rail above. The vibrations induced by the HST moving load inside the GRSP railway system with an AC layer are attenuated on average 1.05 times faster than that inside the standard GRSP railway system with depth.

#### 4.2. Influence of speed variation and overload on a geogrid-reinforced-pile- supported embankment behaviour

The train speed varies during an HST operation, which constantly changes the dynamic behaviour of the railway. The impact of the AC layer on a GRSP railway structure during various changes in the HST speed was studied. Figure 11a shows the vertical dynamic displacement variation at diverse speeds for the standard wheel force of 70 kN. The dynamic displacements peak at the rail top while the HST operates. The vertical dynamic displacement increases with the HST speed, whether the GRSP railway system is with or without an AC layer. The difference between the dynamic displacement in the standard GRSP structure and the dynamic displacement in the GRSP structure with the AC layer expands as the train speed increases, indicating that vibration accentuation of the system depends strongly on the HST moving speed. Besides, the vertical dynamic displacement of the GRSP structure with the AC layer below the vertical dynamic displacement of the standard GRSP structure is subjected to the same train speed. As the speed increases, the difference between the dynamic displacement value of the standard GRSP and the one of the GRSP with AC becomes noticeable. When the speed is 400 km/h, the maximum vertical dynamic displacement of the GRSP structure with the AC layer and the standard GRSP structure is 1.51 mm and 1.74 mm, respectively; the dynamic displacement reduction is 13.21%. Moreover, the line formed by the junction of maximum dynamic displacements for the GRSP structure with AC is closer to the horizontal than that of the standard



Note: target train speed – 200 km/h; wheel load – 70 kN  
**Figure 9.** Vertical dynamic displacement at rail top



Note: target train speed – 200 km/h; wheel load – 70 kN  
**Figure 10.** Maximum vertical dynamic displacement with depth

GRSP structure. The disparity between the dynamic displacement of the standard GRSP and the one of the GRSP with AC during the speed variation was summarized in Table 6 to better understand the graph interpretation by considering four speeds type.

The disparity of dynamic displacements is much more significant during the speed variation when the GRSP system lacks an AC layer. Trying to calculate an imaginary slope caused by the maximum dynamic displacement variation when the HST moves at 100 km/h, then at 400 km/h, a slope of  $2.46 \cdot 10^{-4}$  for the GRSP structure with AC layer and a slope of  $6.53 \cdot 10^{-4}$  for the standard GRSP structure. The slope is 2.65 times lower when an AC layer is present in a GRSP railway system. The observed slope reduction allows passengers to experience less turbulence due to speed changes during train operation. Thus, inserting an AC layer in railway construction is essential to regularize the system vibrations and maintain the low vibration despite the HST speed variation during its operation.

Being overweight during travel is a frequent problem in transportation. The railway system behaviour under various dynamic loads was studied. Figure 11b shows the vertical dynamic displacement variation at the rail top surface when a wheel load is 70 kN, 120 kN, 170 kN, and 220 kN. The maximum vertical dynamic displacements at the rail top surface while the HST moves at 200 km/h are compared. Regardless of the GRSP structure or GRSP structure with the AC layer, the vertical dynamic displacement gradually increases as the HST wheel load increases, which indicates that overloading increases

Table 6. Recapitulative of maximum dynamic displacement at the rail top surface

Type of structure	Maximum dynamic displacement in the function of speed in mm, km/h				The disparity in dynamic displacement during speed change of high-speed train, km/h		
	100	200	300	400	100–200	200–300	300–400
Standard geogrid-reinforced-pile supported structure	1.546	1.589	1.647	1.742	0.043	0.058	0.095
Geogrid-reinforced-pile-supported embankment structure with asphalt concrete layer	1.438	1.457	1.485	1.512	0.0019	0.028	0.027

the deformation of the rail. Besides, the difference in displacement between the two structures, caused by a similar wheel load, becomes more significant when the wheel load is large. The maximum dynamic displacement of the GRSP structure with the AC layer and the standard GRSP structure is 3.97 mm and 4.99 mm, respectively, implying a displacement reduction rate of 20.44% when the load at the wheel is 220 kN. Thus, the AC material plays a crucial role in reducing the displacement of the structure due to being overweight.

### 4.3. The effect of weather conditions on the behaviour of a geogrid-reinforced-pile embankment with asphalt concrete

The dynamic strain and stress at the AC layer top surface were computed considering weather conditions to investigate the environmental conditions influencing the AC material performance to improve the GRSP system response during an HST passage. Figures 12a and 12b illustrate the time history of the stress and the strain at the

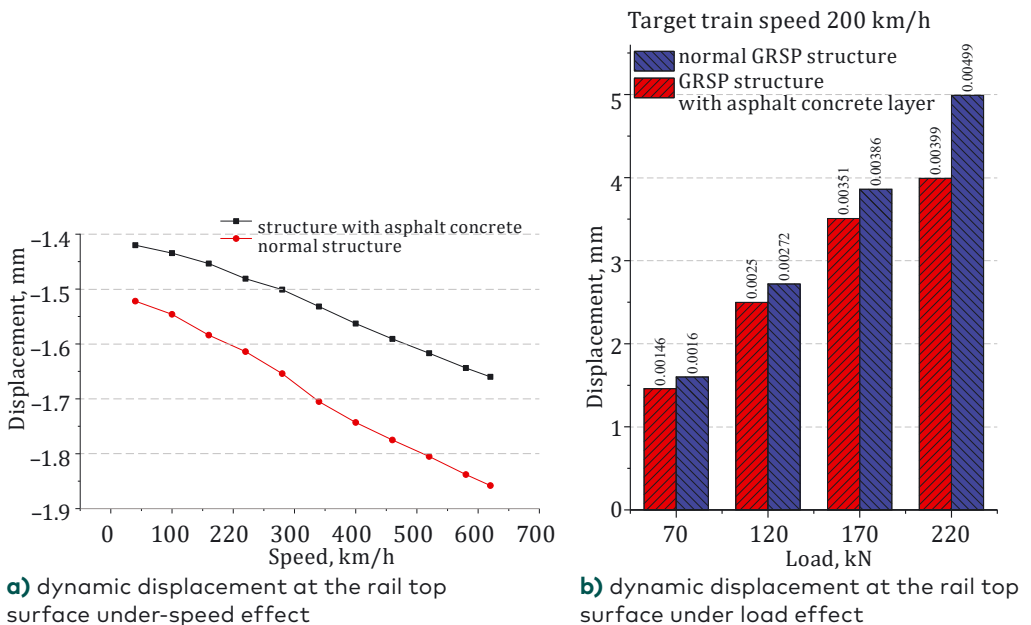
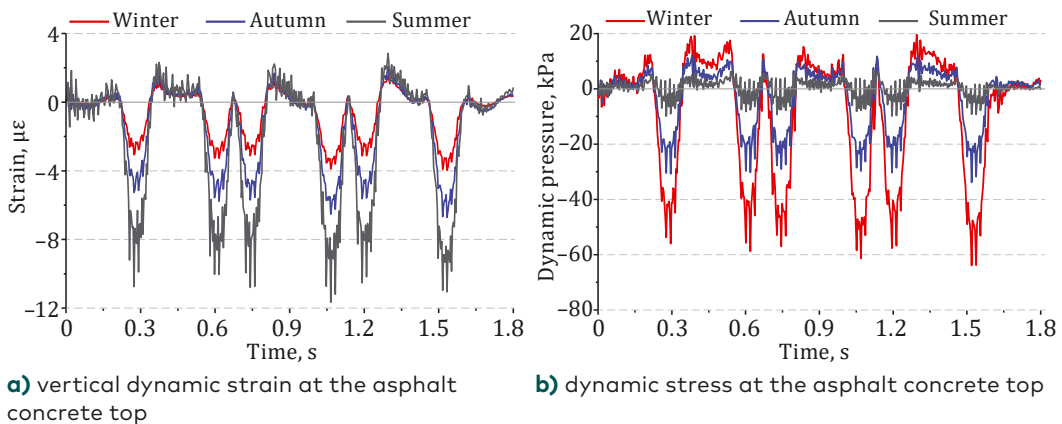


**Figure 11.** Maximum vertical dynamic displacement at the rail top

top of the AC layer, when the HST speed was 200 km/h, under different weather conditions. The dynamic strain and stress time histories in diverse temperature conditions have the same curve form and the same tendency to change with time. However, their maximum values change from one temperature condition to another. The dynamic strain and the dynamic stress at the AC layer top surface for each temperature condition have a tensile and compressive component. The maximum dynamic strain computed at the AC layer top surface decreases significantly in winter. For instance, with the decrease in temperature, the vertical dynamic strain induced by the HST passage decreased from 11.660  $\mu\epsilon$  to 3.969  $\mu\epsilon$ . Inversely, the dynamic pressure increased from 9.907 kPa to 63.898 kPa. From the above results, due to the viscoelastic characteristics of the AC layer, the GRSP railway system performance is improved in winter during the HST operation. The dynamic strain was reduced by 65.97% from summer to winter. Concerning the dynamic pressure, the stress borne by the AC layer in winter is 6.4 times higher than that in summer. Therefore, the AC layer bears more stress in winter than in summer. This phenomenon is due to asphalt viscoelastic behaviour, which becomes more resistant as the freshness increases. Thus, the climate nullifies the role of AC material as a rigid platform to withstand the dynamic load of the train.



Note: target train speed – 200 km/h; wheel load – 70 kN

**Figure 12.** Dynamic stress and strain at the asphalt concrete top

## Conclusions

In this study, the structural behaviour of geogrid-reinforced-pile-supported embankment railroad structure, in which the embankment top layer portion was replaced with an asphalt concrete layer, has been investigated. A 3D nonlinear finite element of the instrumented geogrid-reinforced-pile-supported embankment railway system was established to simulate its mechanical response under different moving speeds, wheel load levels, and temperature conditions. The high-speed train moving wheel load was defined as a transitory dynamic load via a subroutine developed in Fortran. The finite element model reliability was proved by comparing the results with the data obtained from the field tests performed on the Harbin–Dalian railway section. This study led to some results summarized as follows:

1. The dynamic accelerations and stress computed by the established 3D nonlinear geogrid-reinforced-pile-supported embankment finite element model are consistent with those measured at the Harbin–Dalian railroad section in China. Furthermore, the correlation analysis between the computed and measured response indicated that the assumption made in establishing this 3D nonlinear geogrid-reinforced-pile-supported embankment finite element model on the accuracy of the numerical model is relatively insignificant. The developed finite element model can accurately predict the geogrid-reinforced-pile-supported embankment railway system dynamic behaviour taking into account the rail top surface irregularity.

2. An assessment of the asphalt concrete layer impact on the geogrid-reinforced-pile-supported embankment railway system dynamic response revealed that the asphalt concrete layer reduces the dynamic displacement at the rail top surface by 9%. Likewise, the vibration attenuation along the geogrid-reinforced-pile-supported embankment railway system in depth is on average 1.05 times faster. Overall, replacing the embankment top portion with an asphalt concrete layer enhances the geogrid-reinforced-pile-supported embankment railway system performance by minimizing the vibrations while the train operates.

3. Using the asphalt concrete in the geogrid-reinforced-pile-supported embankment railway construction improves the system dynamic response. Thus, the track vibrations due to the high-speed train speed variation are reduced. For instance, from 100 km/h to 400 km/h, an imaginary slope created by the variation of the maximum displacement due to the speed changes is 2.65 times reduced when the asphalt concrete is incorporated in the

geogrid-reinforced-pile-supported embankment structure design. This phenomenon improves the comfort of passengers, sometimes perturbed by the variation of the system vibrations due to the changes in the high-speed train speeds during its operation. This material is essential to regulate the structural vibrations and maintain the low vibration level despite the speed variation during the high-speed train operation, which guarantees passenger comfort.

4. Overloading is a phenomenon that is very frequent in rail transport, especially since the weight of luggage is sometimes uncontrolled in stations. Thus, the use of asphalt in the railway structure slows down roadway degradation by reducing excessive vibrations due to overloads.

5. Although the viscoelastic characteristics of asphalt concrete material make, its behaviour stalwartly depends on temperature. However, its presence in the top part of the geogrid-reinforced-pile-supported embankment system embankment was found insignificant to affect the geogrid-reinforced-pile-supported embankment railway system performance. In winter, the asphalt concrete layer deforms less and bears 6.4 times of stress than in summer due to the dynamic trainload.

## Acknowledgements

The authors of this scientific work and this paper gratefully acknowledge the financial support for this research from the National Key R&D Program of China (Grants No. 2016YEE0205100 and No. 2018YFC1505305), State Key Program of the National Natural Science Foundation of China (Grant No. 41430634 and No. 41731288), the National Major Scientific Instruments Development Project of China (Grant No. 41627801), and the Technology Research and Development Plan Program of Heilongjiang Province (Grant No. GA19A501).

## Funding

This work was supported by the National Key R&D Program of China (Grants No. 2016YEE0205100 and 2018YFC1505305), the State Key Program of the National Natural Science Foundation of China (Grant No. 41430634 and No. 41731288), the National Major Scientific Instruments Development Project of China (Grant No. 41627801), and the Technology Research and Development Plan Program of Heilongjiang Province (Grant No. GA19A501).

## REFERENCES

- Abaqus, G. (2011). Abaqus 6.11. *Dassault Systemes Simulia Corporation, Providence, RI, USA*.
- Assogba, O. C., Tan, Y., Sun, Z., Lushinga, N., & Bin, Z. (2021). Effect of vehicle speed and overload on dynamic response of semi-rigid base asphalt pavement. *Road Materials and Pavement Design*, 22(3), 572-602. <https://doi.org/10.1080/14680629.2019.1614970>
- Assogba, O. C., Tan, Y., Zhou, X., Zhang, C., & Anato, J. N. (2020). Numerical investigation of the mechanical response of semi-rigid base asphalt pavement under traffic load and nonlinear temperature gradient effect. *Construction and Building Materials*, 235, 117406. <https://doi.org/10.1016/j.conbuildmat.2019.117406>
- Bian, X., Jiang, H., Chang, C., Hu, J., & Chen, Y. (2015). Track and ground vibrations generated by high-speed train running on ballastless railway with excitation of vertical track irregularities. *Soil Dynamics and Earthquake Engineering*, 76, 29-43. <https://doi.org/10.1016/j.soildyn.2015.02.009>
- Chango, I. V. L., Yan, M., Ling, X., Liang, T., & Assogba, O. C. (2019). Dynamic response analysis of geogrid reinforced embankment supported by CFG pile structure during a high-speed train operation. *Latin American Journal of Solids and Structures*, 16(7), 1-20.
- Chen, J., & Zhou, Y. (2018). Dynamic responses of subgrade under double-line high-speed railway. *Soil Dynamics and Earthquake Engineering*, 110, 1-12.
- Devecseri, G. (2010). Effect of heating on the physical properties of asphalt aggregates. *Periodica Polytechnica Civil Engineering*, 54(1), 53-60. <https://doi.org/10.3311/pp.ci.2010-1.06>
- Fang, M., & Cerdas, S. F. (2015). Theoretical analysis on ground vibration attenuation using sub-track asphalt layer in high-speed rails. *Journal of Modern Transportation*, 23(3), 214-219. <https://doi.org/10.1007/s40534-015-0081-3>
- Fang, M., Cerdas, S. F., & Qiu, Y. (2013). Numerical determination for optimal location of sub-track asphalt layer in high-speed rails. *Journal of Modern Transportation*, 21(2), 103-110. <https://doi.org/10.1007/s40534-013-0012-0>
- Fang, M., Qiu, Y., Rose, J. G., West, R. C., & Ai, C. (2011). Comparative analysis on dynamic behavior of two HMA railway substructures. *Journal of Modern Transportation*, 19(1), 26-34. <https://doi.org/10.1007/BF03325737>
- Gailienė, I., & Ramūnas, V. (2019). Usage analysis and evaluation of slab track constructions. *The Baltic Journal of Road and Bridge Engineering*, 14(3), 285-303. <https://doi.org/10.7250/bjrbe.2019-14.444>
- Gao, J., & Zhai, W. (2014). Dynamic effect and safety limits of rail weld irregularity on high-speed railways. *SCIENTIA SINICA Technologica*, 44(7), 697-706. <https://doi.org/10.1177/0954409716664933>
- Hu, S., Zhou, F., & Walubita, L. F. (2009). Development of a viscoelastic finite element tool for asphalt pavement low temperature cracking analysis. *Road Materials and Pavement Design*, 10(4), 833-858. <https://doi.org/10.1080/14680629.2009.9690229>

- Lee, S. H., Lee, J. W., Park, D. W., & Vo, H. V. (2014). Evaluation of asphalt concrete mixtures for railway track. *Construction and Building Materials*, 73, 13-18. <https://doi.org/10.1016/j.conbuildmat.2014.09.053>
- Liu, L., & Shao, W. (2011). Design and dynamic response analysis of rail with constrained damped dynamic vibration absorber. *Procedia Engineering*, 15, 4983-4987. <https://doi.org/10.1016/j.proeng.2011.08.926>
- Minhoto, M. J., Pais, J. C., & Pereira, P. A. (2008). The temperature effect on the reflective cracking of asphalt overlays. *Road Materials and Pavement Design*, 9(4), 615-632. <https://doi.org/10.1080/14680629.2008.9690141>
- Park, S. W., & Schapery, R. (1999). Methods of interconversion between linear viscoelastic material functions. Part I—a numerical method based on Prony series. *International Journal of Solids and Structures*, 36(11), 1653-1675. [https://doi.org/10.1016/S0020-7683\(98\)00055-9](https://doi.org/10.1016/S0020-7683(98)00055-9)
- Rose, J. G. (2013, April). Selected in-track applications and performances of hot-mix asphalt trackbeds. In *ASME/IEEE Joint Rail Conference* (Vol. 55300, p. V001T01A017). American Society of Mechanical Engineers. <https://doi.org/10.1115/JRC2013-2525>
- Schapery, R. A., & Park, S. W. (1999). Methods of interconversion between linear viscoelastic material functions. Part II—an approximate analytical method. *International Journal of Solids and Structures*, 36(11), 1677-1699. [https://doi.org/10.1016/S0020-7683\(98\)00060-2](https://doi.org/10.1016/S0020-7683(98)00060-2)
- Sun, Q., Zhang, X. D., Yang, Y., & Liu, J. S. (2013). Research on settlement of pile-net composite foundation of high-speed railway in soft soil area. *Guangxi Daxue Xuebao (Ziran Kexue Ban)*, 38(1): 157-164.
- Sysyn, M. P., Kovalchuk, V. V., Nabochenko, O. S., Kovalchuk, Y., & Voznyak, O. M. (2019). Experimental study of railway tracked pressure distribution under dynamic loading. *The Baltic Journal of Road and Bridge Engineering*, 14(4): 504-520. <https://doi.org/10.7250/bjrbe.2019-14.455>
- Williams, M. L., Landel, R. F., & Ferry, J. D. (1955). The temperature dependence of relaxation mechanisms in amorphous polymers and other glass-forming liquids. *Journal of the American Chemical Society*, 77(14), 3701-3707. <https://doi.org/10.1021/ja01619a008>
- Yang, E., Wang, K. C., Luo, Q., & Qiu, Y. (2015). Asphalt concrete layer to support track slab of high-speed railway. *Transportation Research Record*, 2505(1), 6-14. <https://doi.org/10.3141/2505-02>
- Yang, J., Kong, B., Cai, C. S., & Wang, J. S. (2016). Behavior of high-speed railway ballastless track slabs using reactive powder concrete materials. *Journal of Transportation Engineering*, 142(8), 04016031. [https://doi.org/10.1061/\(ASCE\)TE.1943-5436.0000849](https://doi.org/10.1061/(ASCE)TE.1943-5436.0000849)
- Yusupov, B., Qiu, Y., Ding, H., & Rahman, A. (2020). Temperature and material behaviour effects on dynamic responses of asphalt concrete trackbed. *International Journal of Rail Transportation*, 8(1), 66-79. <https://doi.org/10.1080/23248378.2019.1628671>
- Zakeri, J. A., Feizi, M. M., Shadfar, M., & Naeimi, M. (2017). Sensitivity analysis on dynamic response of railway vehicle and ride index over curved bridges. *Proceedings of the Institution of Mechanical Engineers, Part K: Journal of Multi-Body Dynamics*, 231(1), 266-277.

<https://doi.org/10.1177/1464419316662568>  
Zienkiewicz, O. C., Taylor, R. L., & Zhu, J. Z. (2005). *The Finite Element Method: Its Basis and Fundamentals*. Elsevier.

**Ishola Valere Loic  
Chango,  
Goubi Cyriaque  
Assogba,  
Muhan Yan,  
Ling Xianzhang,  
Josue Girece  
Mitobaba**

Impact Assessment  
of Asphalt Concrete  
in Geogrid-  
Reinforced-  
Pile-Supported  
Embankment  
During High-Speed  
Train Traffic